Hindawi
Shock and Vibration
Volume 2021, Article ID 2522386, 15 pages
https://doi.org/10.1155/2021/2522386

Research Article

Abnormal Wear Mechanism and Improvement of High-Speed Cylindrical Roller Bearing

Wenhu Zhang,[1,2] Sier Deng ,[1,3] Song Zhang,[3] Jian Wang,[4] and Jintao Zheng[1]

[1]*School of Mechatronics Engineering, Henan University of Science and Technology, Luoyang 471003, China*
[2]*National United Engineering Laboratory for Advanced Bearing Tribology, Henan University of Science and Technology, Luoyang 471003, China*
[3]*Post-Doctoral Research Centre of Changzhou NRB Corporation, Changzhou 213022, China*
[4]*Luoyang Bearing Research Institute Co., Ltd, Luoyang 471003, China*

Correspondence should be addressed to Sier Deng; dse@haust.edu.cn

Received 13 May 2021; Revised 10 July 2021; Accepted 15 July 2021; Published 26 July 2021

Academic Editor: S bastien Besset

This paper presents the dynamic differential equations of cylindrical roller bearing, considering the dynamic unbalance mass of roller and the contact between the roller end face and the inner ring rib. The influence of bearing working condition and structural parameters on the *PV* value of roller end face and the slip speed of roller working surface were analysed. The theoretical analysis and experimental results both show that the large amount of roller's dynamic unbalance mass due to the difference in chamfering size on both sides of the roller and the deviation of the bearing axial clearance are the main causes of abnormal wear on the roller working surface and end face.

1. Introduction

The primary failure modes of high-speed cylindrical roller bearing under light load are the skidding of roller and the fracture of cage [1, 2]. There is a lack of research on bearing failures caused by the serious wear of roller working surface and end faces, named "abnormal wear of roller" in the paper, which cannot provide a theoretical support for bearing fault location and optimization design.

Yang et al. [3] analysed the wear of roller end face in high-speed cylindrical roller bearing and obtained the interconnection between the influencing factors and solved the wear of roller end face. Based on discrete mathematics and computer technology, Shi et al. [4, 5] established a numerical wear simulation model of cylindrical roller bearing, considering the time-varying characteristics of contact pressure and spin speed, to predict its wear life and reliability. Yao et al. [6] analysed the bearing with different degrees of wear failure through the whole simulation model of bearing, revealed the failure process of bearing and the characteristic value of failure fault, and carried out the experiment verification. The results showed that the concentration of the base vibration signal spectrum can reflect the degree of bearing wear and tear. Yu et al. [7] analysed the wear phenomenon of the roller end face and inner ring rib during the operation of an aero-engine cylindrical roller bearing and deemed that the main reason is the insufficient precision control of roller and inner ring rib. Accordingly, improvement for reducing the tolerance range of roller chamfers and increasing the angle of inner ring rib was proposed. Based on the working conditions and structural characteristics of a certain type of aero-engine intermediary bearing, Wen [8] determined that the main reason for the wear of the roller end face is the unbalanced torque caused by the high-speed operation of the roller, and the frequent contact between the roller and the inner ring rib and the cage pocket leads to the torsion pendulum of the roller back and forth. The axial clearance and radial clearance range of bearing are improved reasonably based on the geometric relation of cylindrical roller bearing. Aditya et al. [9] developed an experimental test rig to investigate the wear in a grease-lubricated cylindrical roller bearing and studied the

influence of bearing temperature, misalignment, and roughness on the lubricant film thickness. Han et al. [10] presented a nonlinear dynamic model for skidding behaviour of cylindrical roller bearing, considering the radial clearance, roller crown profile, and discontinuous contact between the roller and cage to study the roller's skidding behaviour under the time-variable load condition. Zhang et al. [11] investigated the skidding damage dynamic behaviours of cylindrical roller bearing using a high-speed rolling bearing test rig and revealed the skidding damage mechanism and the failure characteristics. Li et al. [12] proposed a new damage-mechanics-based model for rolling contact fatigue analysis in terms of the amplitude of octahedral shear stress, considering the nonproportional variation of stress, and the material parameters and simulated the crack initiation, crack propagation, and spalling in the working process of cylindrical roller bearing. Tu et al. [13] proposed a dynamic model to investigate the vibration of cylindrical roller bearing considering skidding, of which the generating mechanism is explained, and it is found that the existence of skidding may lead to fluctuations and a significant increase of the friction force, which will increase the vibration level and introduce impact components into the vibration. In addition, according to the analysis of the dynamic characteristics of cylindrical roller bearing, many scholars have also discussed many aspects: The dynamic characteristics of load distribution, oil film thickness, roller and cage slip, roller skew, and axial movement were calculated, and the nonlinear dynamic model of cylindrical roller bearing was established by Leblanc et al. [14], considering the structural deformation of the ring and cage material, the force and torque produced by the roller raceway contact were analysed, and the nonlinear dynamic model of high-speed cylindrical roller bearing was established by Wang et al. [15]. Yongcun et al. [16, 17] established a dynamics model of cylindrical roller bearing considering roller's dynamic unbalance mass and studied the effects of roller's dynamic unbalance mass on cage nonlinear dynamic characteristics, especially on cage vibration. Sun et al. [18,19] established the nonlinear dynamic differential equations of cylindrical roller bearings with an elastic ring and studied the effect of the elastic ring on the slip ratio and stability of cage. Liu et al. [20] developed a coupled model of roller tilt and skew, considering thermal effects and non-Newtonian characteristic lubricants, to study the effect of roller tilt and skew on thermal elastohydrodynamic lubrication. Zhang et al. [21] proposed the dynamic differential equations of high-speed cylindrical roller bearing, considering the effect of roller convexity offset on roller mass centre and the effect of convexity offset on the tilt angle and skew angle of the roller under four different methods and different speeds and loads were studied. Patra et al. [22] used the Lagrange equation to establish a dynamic model of cylindrical roller bearing by using the improved Newmark-β method to solve the numerical problem; the dynamic characteristics of cylindrical roller bearing in an equilibrium and unbalanced state are studied. Aiming at the atypical failure problem of cylindrical roller bearing in an aero-engine, Zheng et al. [23] established the dynamic differential equations of high-speed cylindrical roller bearing by taking into account the contact behaviour between the roller with dynamic unbalanced mass and inner ring rib. The influence of the bearing parameters on the maximum skew angle of roller and the maximum collision force between the roller and rib were analysed. The above studies mainly focused on the failure analysis, improved design, and bearing dynamic performance of cylindrical roller bearing; however, the wear mechanisms of roller end faces and end surface have not been studied. The solution to the abnormal wear of the roller working surface and end face cannot be put forward from the root.

In this paper, a dynamic simulation analysis model of cylindrical roller bearing is carried out by considering the dynamic unbalance mass of roller and contact between the roller end face and inner ring rib. The wear degree of roller end face and roller working surface are characterized by the PV value and roller's slip speed, respectively. This study investigates the key factors affecting the wear of roller end face and working surface and reveals the formation mechanism of abnormal wear. It provides a theoretical support for the troubleshooting and structural optimization design of cylindrical roller bearing under high speed and light load.

2. Characterization of Wear Failure of the Bearing

The wear of roller working surface and end faces after the bearing test is shown in Figure 1. These failure modes are not common in the same type of bearing test and host application. Based on our experience, it is suspected that the difference in chamfering size on both sides of the roller and the deviation of bearing axial clearance are the main causes; however, the abnormal wear mechanism of roller and the optimization design of bearing are not clear. Bearing faults are difficult to solve.

3. Dynamic Model of High-Speed Cylindrical Roller Bearing

3.1. Coordinate System of the Cylindrical Roller Bearing. To accurately describe the motion state of each component of cylindrical roller bearing and the interaction relationship between the components, the coordinate systems of cylindrical roller bearing are shown in Figure 2. The coordinate systems include the following:

(1) *Inertial Coordinate System* $(O; X, Y, Z)$. The origin O is located in the geometric centre of outer ring, the X-axis coincides with outer ring axis, and the YOZ plane is parallel to the radial plane of outer ring. The outer ring is fixed during the operation of bearing; that is, the inertial coordinate system is fixed in space.

(2) *Inner Ring Centroid Coordinate System* (o_i, x_i, y_i, z_i). The origin o_i coincides with inner ring centroid, the x_i axis is parallel to the inertial coordinate system X-axis, the $y_i o_i z_i$ plane is parallel to the radial plane of

(a) (b)

Figure 1: Examples of high-speed cylindrical roller bearing failures.

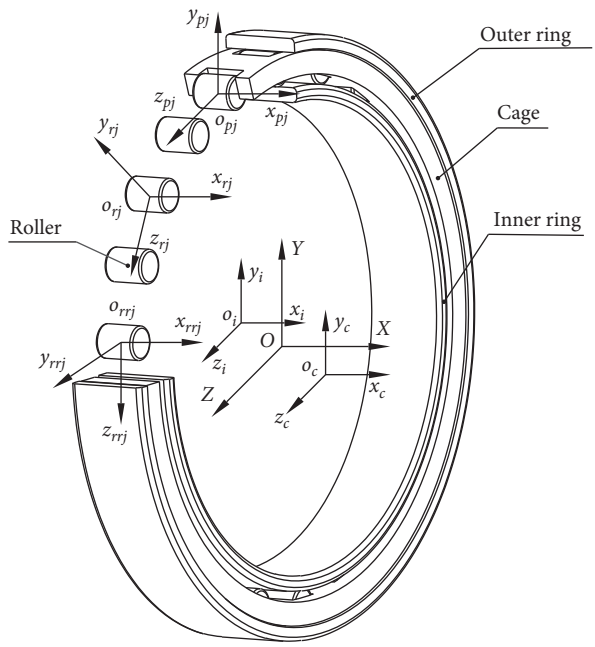

Figure 2: Coordinate systems of the cylindrical roller bearing.

inner ring, and this coordinate system moves and rotates with inner ring.

(3) *Cage Centroid Coordinate System* $(o_c; x_c, y_c, z_c)$. The origin o_c coincides with the cage centroid, the x_c axis is parallel to the inertial coordinate system X-axis, the $y_c o_c z_c$ plane is parallel to the radial plane of cage, and this coordinate system moves and rotates with the cage.

(4) *Cage Pocket Coordinate System* $(o_{pj}; x_{pj}, y_{pj}, z_{pj})$. The origin o_{pj} coincides with the centre of the j pocket of cage, the x_{pj} axis is parallel to the inertial coordinate system X-axis, the $y_{pj} o_{pj} z_{pj}$ plane is parallel to the cage radial plane, the y_{pj} axis passes through the cage centre, and this coordinate system moves and rotates with the cage.

(5) *Roller Centre Coordinate System* $(o_{rj}; x_{rj}, y_{rj}, z_{rj})$. The origin o_{rj} coincides with the jth roller geometric centre, the x_{rj} axis is along the axis direction of the jth roller, the $y_{rj} o_{rj} z_{rj}$ plane is parallel to the radial plane of the jth roller, and this coordinate system moves and rotates with the roller.

(6) *Roller Reference Coordinate System* $(o_{rrj}; x_{rrj}, y_{rrj}, z_{rrj})$. The origin o_{rrj} coincides with the jth roller geometric centre, the x_{rrj} axis is parallel to the X-axis of the inertial coordinate system, the $y_{rrj} o_{rrj} z_{rrj}$ plane is parallel to the YOZ plane of the inertial coordinate system, and this coordinate system moves and rotates with the roller.

3.2. Analysis on the Force between Roller End Face and Inner Ring Rib. The outer ring of cylindrical roller bearing has no rib, and the inner ring has double ribs. When the skew angle of roller is large, the contact between the roller end face and inner ring rib occurs [24], and the contact and geometric relationships are shown in Figure 3.

From the geometric relationship [25], the elastic deformation between the roller end face and the unilateral rib of inner ring is given in the following equation:

$$\delta_{\mathrm{L}}^{K} = \left[(1 - \cos\ \alpha_{\mathrm{r}}) \cdot \left(R_{\mathrm{p}} - \frac{L_{\mathrm{p}}}{2} \right) - \left(\frac{C_{\mathrm{a}}}{2} + C_{\mathrm{af}} \right) + X_r^K \right] \cdot \cos\ \theta_{\mathrm{f}}, \tag{1}$$

where the calculation corresponds to the left side when K is equal to L and to the right side when K is equal to R; α_{r} is the skew angle of roller; C_{a} is bearing axial clearance; R_{p} is the distance between the contact point and the crowned centre of roller end face in the $x_{\mathrm{r}j}$ direction.

$$R_{\mathrm{p}} = R_{\mathrm{s}} \cdot \cos\ \theta_{\mathrm{f}}. \tag{2}$$

Equation (3) gives the length of the roller L_{p} in the plane, parallel to the $x_{\mathrm{r}j} o_{\mathrm{r}j} z_{\mathrm{r}j}$ surface where the contact point is located.

$$L_{\mathrm{p}} = L_{\mathrm{r}} - 2\left(R_{\mathrm{s}} - R_{\mathrm{p}} \right), \tag{3}$$

where R_{s} is the crowned radius of roller end face, L_{r} is the length of roller, and C_{af} is the unilateral axial clearance caused by the angle of rib θ_{f}.

$$C_{\mathrm{af}} = \left(H_{\mathrm{rollercm}} - \frac{D_{\mathrm{w}}}{2} \right) \cdot \tan\ \theta_{\mathrm{f}}, \tag{4}$$

where H_{rollercm} is the distance between the centre of roller and the raceway of inner ring and D_{w} is the diameter of roller.

X_{r}^K is the gap increment caused by the axial displacement of roller.

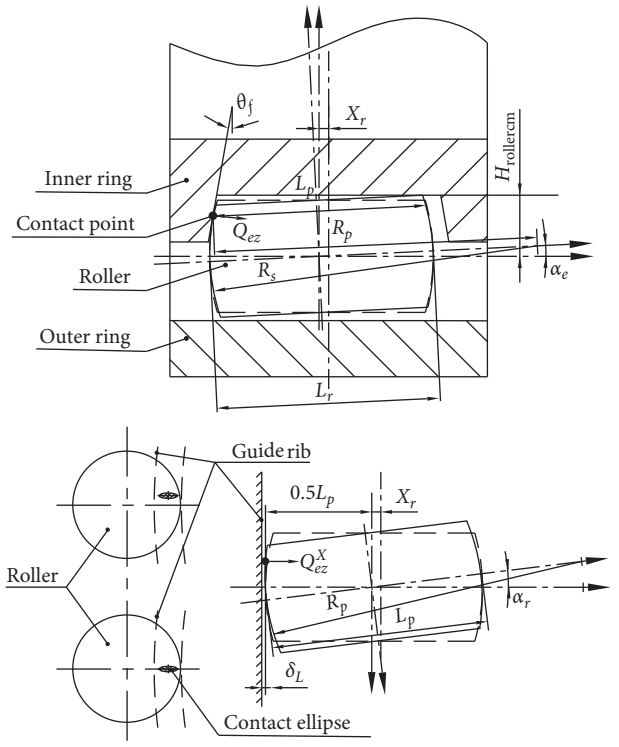

Figure 3: Contact and geometric relationship between the roller end face and inner ring rib.

$$\begin{cases} X_{\mathrm{r}}^{L} = -X_{\mathrm{r}}, \\ X_{\mathrm{r}}^{R} = X_{\mathrm{r}}, \end{cases} \tag{5}$$

where X_{r} is the displacement of roller relative to the mass centre of inner ring in the X-axis direction of inertial coordinate system.

According to the Hertz point contact theory, the normal contacts force between ribs and roller end faces is determined [26, 27].

$$Q_{ez}^{K} = \frac{\pi E' k}{3}\left[2R_{eff}\Pi\left(\frac{\delta_{\mathrm{L}}^{K}}{\Gamma}\right)^{3}\right]^{1/2}, \tag{6}$$

where E' is the comprehensive elastic modulus of materials for the roller and inner ring and k is the ratio of the semimajor axis to the semiminor axis of contact ellipse, given by the following equation:

$$k = 1.0339\left(\frac{R_y}{R_x}\right)^{0.636}. \tag{7}$$

R_{eff} is the equivalent radius of curvature of the contact point.

$$R_{\mathrm{eff}} = \frac{1}{\left(1/R_x + 1/R_y\right)}. \tag{8}$$

Γ and Π are the first kind of complete elliptic integral and the second kind of complete elliptic integral, respectively.

$$\begin{aligned} \Gamma &= 1.0003 + \frac{0.5968}{\left(R_y/R_x\right)}, \\ \Pi &= 1.5277 + 0.6023\ \ln\left(R_y/R_x\right), \end{aligned} \tag{9}$$

where R_x and R_y are the equivalent radii of curvature in the two orthogonal planes where the contact point is located.

$$\begin{cases} R_x = \dfrac{1}{\left\{1/R_{\mathrm{s}} + 1/\left[\left(d_{\mathrm{i}}/2 + H_{\mathrm{contact}}\right)/\tan\ \theta_{\mathrm{f}}\right]\right\}}, \\ R_y = R_{\mathrm{s}}, \\ \dfrac{R_y}{R_x} \geq 1, \end{cases} \tag{10}$$

where H_{contact} is the height of the contact point between roller end face and rib.

$$H_{\mathrm{contact}} = H_{\mathrm{rollercm}} - R_s \cdot\ \sin\ \theta_f + 0.5L_r \cdot\ \sin\ \alpha_e, \tag{11}$$

where α_{e} is the tilt angle of roller.

The friction force between roller end face and one rib is given in the following equation:

$$Q_{\mathrm{e}\theta}^{K} = C \cdot \left(F_{\mathrm{G}} + \mu Q_{ez}^{K}\right), \tag{12}$$

where μ is the friction coefficient between the roller end face and inner ring rib and C is the direction of μ, which is determined by the following equation:

$$\begin{cases} C = +1, & v_{\mathrm{i}} \geq v_{\mathrm{r}}, \\ C = -1, & v_{\mathrm{i}} < v_{\mathrm{r}}, \end{cases} \tag{13}$$

where v_{i} and v_{r} are the linear velocities of rib and roller at the contact point, respectively.

F_{G} is the friction force generated by the lubricant on the roller end face.

$$F_{\mathrm{G}} = \left(\omega_{\mathrm{i}} - \omega_{0j}\right) v \rho_{\mathrm{e}} \int \frac{R}{C_a}\mathrm{d}A, \tag{14}$$

where ω_{i} is the angular velocity of inner ring, ω_{0j} is the orbital angular velocity of the jth roller, v is the kinematic viscosity of lubricant, and ρ_{e} is the oil/gas density.

$$\int \frac{R}{C_a}\mathrm{d}A = \frac{4}{3}\frac{R_0}{C_{\mathrm{a}}} h_{\mathrm{f}} \sqrt{\left(\frac{D_{\mathrm{w}}}{2}\right)^2 - \left(\frac{D_{\mathrm{w}}}{2}\right)^2}, \tag{15}$$

where R_0 is the radius of the contact point and h_{f} is the height of rib. In summation, the overall forces and torques acting on the jth roller's end faces by double ribs of inner ring are determined.

$$\begin{cases} Q_{ez}^{X} = \left(Q_{ez}^{L} - Q_{ez}^{R}\right)\cos\ \theta_{\mathrm{f}}, \\ Q_{ez}^{Y} = \left(Q_{ez}^{L} + Q_{ez}^{R}\right)\sin\ \theta_{\mathrm{f}}, \\ Q_{\mathrm{e}\theta} = Q_{\mathrm{e}\theta}^{L} + Q_{\mathrm{e}\theta}^{R}, \\ M_{e\theta x} = \left(Q_{e\theta}^{L} + Q_{e\theta}^{R}\right) \cdot \left(H_{\mathrm{rollercm}} - H_{\mathrm{contact}}\right) - 2M_{\mathrm{G}}, \\ M_{e\theta} = \left(Q_{e\theta}^{L} - Q_{e\theta}^{R}\right) \cdot \left(\frac{L_p}{2} + \frac{C_a}{2}\right), \\ M_{er} = \left(Q_{ez}^{L} + Q_{ez}^{R}\right)\cos\ \theta_{\mathrm{f}} \cdot \left(R_p - \frac{L_{\mathrm{p}}}{2}\right)\sin\ \alpha_{\mathrm{r}}, \\ M_{ee} = \left(Q_{ez}^{L} + Q_{ez}^{R}\right)\sin\ \theta_{\mathrm{f}} \cdot \left(\frac{L_{\mathrm{p}}}{2}\right)\sin\ \alpha_{\mathrm{e}}, \end{cases} \tag{16}$$

where Q_{ez}^{X} and Q_{ez}^{Y} are the components along the x_{rrj} and y_{rrj} directions in $(o_{\mathrm{rr}j}; x_{\mathrm{rr}j}, y_{\mathrm{rr}j}, z_{\mathrm{rr}j})$, respectively; $Q_{e\theta}$ is the friction force acting on roller end face; $M_{e\theta x}$ and $M_{e\theta}$ are the additional moments generated by $Q_{e\theta}$; M_{er} and M_{ee} are the additional moments generated by Q_{ez}^{X} and Q_{ez}^{Y}; M_{G} is the moment generated by the lubricant acting on roller end face.

$$M_G = F_G \cdot \left(\frac{D_w}{2} - \frac{h_f}{2}\right). \tag{17}$$

4. Dynamic Differential Equations of the Roller

The outer ring is fixed, while the inner ring rotates at a constant speed. The cage is guided by the inner ring, and the inner ring only bears a pure radial load during the operation. When bearing runs at a high speed, the dynamic unbalance mass of roller causes it to bear the additional dynamic load, which causes roller skew and tilt. As shown in Figure 4, suppose that the dynamic unbalance mass of roller O_{mj} is located at an angle θ_{mj} in the axial direction $x_{\mathrm{r}j}$ and an angle $\varphi_{\mathrm{m}j}$ in the radial direction $y_{\mathrm{r}j}$, the distance between O_{mj} and o_{rj} is e_{mj}, F_{cvj} and F_{cwj} are the centrifugal forces generated by the jth roller's dynamic unbalance mass, and the calculated expressions can be found in the literature [16, 17].

During the operation of bearing, the roller is acted by the ring, cage, and lubricant. As shown in Figure 5, the forces and torques between roller end face and inner ring rib are obtained by equation (17). N_{rj}^{i} and N_{rj}^{o} are the normal contact forces between the inner and outer raceways and the jth roller; T_{rj}^{i} and T_{rj}^{o} are the drag forces between the inner and outer raceways and the jth roller. M_{Nrj}^{i} and M_{Nrj}^{o} are the additional moments between the inner and outer raceways and the jth roller generated by N_{rj}^{i} and N_{rj}^{o}; M_{Trj}^{i} and M_{Trj}^{o} are the additional moments between the inner and outer raceways and the jth roller generated by T_{rj}^{i} and T_{rj}^{o}; N_{rj}^{c} and F_{rj}^{c} are the normal contact force and tangential friction force between the cage beam and the jth roller; M_{Nrj}^{c} and M_{Frj}^{c} are the additional moments between the jth roller and the cage beam generated by N_{rj}^{c} and F_{rj}^{c}; F_{rj}^{m} is the jth roller centrifugal force; N_{rjm}^{i} and N_{rjm}^{o} are the contact forces between the inner and outer raceways and the mth slice; T_{rjm}^{i} and T_{rjm}^{o} are the drag forces between the inner and outer raceways and the mth slice; N_{rjm}^{c} and F_{rjm}^{c} are the normal contact force and tangential friction force between the cage cross beam and the mth slice; and α_{rj} and α_{ej} are the skew angle and tilt angle of the jth roller. The expressions of the other symbols are in the literature [23].

The nonlinear dynamic differential equations of the jth roller are

$$\begin{cases} m_{rj}\ddot{x}_{rj} = Q_{ezj}^{X} - F_{cwxj} + \mu_{sj}^{i}N_{rj}^{i} + \mu_{sj}^{o}N_{rj}^{o}, \\ m_{rj}\ddot{y}_{rj} = -N_{rj}^{i}\cos\ \varphi_j + N_{rj}^{o}\cos\ \varphi_j - N_{rj}^{c}\sin\ \varphi_j - T_{rj}^{i}\sin\ \varphi_j + T_{rj}^{o}\sin\ \varphi_j - F_{rj}^{c}\cos\ \varphi_j - F_{rj}^{m}\cos\ \varphi_j - Q_{ezj}^{Y}\cos\ \varphi_j - Q_{e\theta j}\sin\ \varphi_j + F_{cwyj}\cos\ \varphi_j + F_{cwzj}\sin\ \varphi_j - F_{cvj}\cos\ \varphi_j, \\ m_{rj}\ddot{z}_{rj} = N_{rj}^{i}\sin\ \varphi_j - N_{rj}^{o}\sin\ \varphi_j - N_{rj}^{c}\cos\ \varphi_j - T_{rj}^{i}\cos\ \varphi_j + T_{rj}^{o}\cos\ \varphi_j + F_{rj}^{c}\sin\ \varphi_j + F_{rj}^{m}\sin\ \varphi_j + Q_{ezj}^{Y}\sin\ \varphi_j - Q_{e\theta j}\cos\ \varphi_j - F_{cwyj}\sin\ \varphi_j + F_{cwzj}\cos\ \varphi_j + F_{cvj}\sin\ \varphi_j, \\ J_{rxj}\dot{\omega}_{rxj} = -T_{rj}^{i}\frac{D_w}{2} - T_{rj}^{o}\frac{D_w}{2} + F_{rj}^{c}\frac{D_w}{2} - M_{e\theta xj} + \Delta M_{xmj}, \\ J_{ryj}\dot{\omega}_{ryj} = M_{Nrj}^{i}\sin\ \varphi_j + M_{Nrj}^{o}\sin\ \varphi_j - M_{Trj}^{i}\sin\ \varphi_j - M_{Trj}^{o}\sin\ \varphi_j + M_{Frj}^{c}\cos\ \varphi_j + M_{erj}\cos\ \varphi_j + M_{eej}\sin\ \varphi_j - M_{e\theta j}\cos\ \varphi_j - \Delta M_{ymj}\cos\ \varphi_j + \Delta M_{zmj}\sin\ \varphi_j, \\ {}_{rzj}\dot{\omega}_{rzj} = M_{Nrj}^{i}\cos\ \varphi_j + M_{Nrj}^{o}\cos\ \varphi_j - M_{Trj}^{i}\cos\ \varphi_j - M_{Trj}^{o}\cos\ \varphi_j - M_{Frj}^{c}\sin\ \varphi_j - M_{erj}\sin\ \varphi_j + M_{eej}\cos\ \varphi_j + M_{e\theta j}\sin\ \varphi_j + \Delta M_{ymj}\sin\ \varphi_j + \Delta M_{zmj}\cos\ \varphi_j, \end{cases} \tag{18}$$

where m_{rj} is the jth roller mass; φ_j is the azimuth angle of the jth roller; $\ddot{y}_{\mathrm{r}j}$ and $\ddot{z}_{\mathrm{r}j}$ are the jth roller's mass centres in the inertial coordinate system of displacement acceleration; J_{rxj}, J_{ryj}, and J_{rzj} are the rotational inertias of the jth roller in the inertial coordinate system; $\dot{\omega}_{rxj}$, μ_{sj}^{i}, and μ_{sj}^{o} are the angular accelerations of the jth roller in the inertial coordinate system; μ_{sj}^{i} and μ_{sj}^{o} are the transverse friction coefficients between the jth roller and the raceway; F_{cwxj}, F_{cwyj}, and F_{cwzj} are the components of $x_{\mathrm{r}j}$ along x_{rj}, y_{rj}, and z_{rj} directions in the roller reference coordinate system; and

ΔM_{mxj}, ΔM_{myj}, and ΔM_{mzj} are the components of additional moments in the inertial coordinate system due to F_{cvj} and F_{cwj}.

5. Dynamic Differential Equations of the Cage

The cage is acted by roller's collision and friction, gravity, guiding surface's collision and friction, and the dragging of lubricant acting on the nonguiding surface and end faces, as shown in Figure 6.

In Figure 6, $(O; Y, Z)$ is the inertial coordinate system; $(o_c; y_c, z_c)$ is the cage centre-of-mass coordinate system; e is the offset of the cage centre of mass relative to the centre of mass of the inner ring, where $e = \sqrt{\Delta_{cy}^2 + \Delta_{cz}^2}$; Ψ_c' is the eccentricity of the force between the guiding surface and the overall coordinate system of the cage; when the inner ring guides the cage, the eccentricity is Ψ_c, where $\Psi_c = \Psi_c' + \pi$; F_{cy} and F_{cz}' are the two orthogonal components of the force between the guiding surface of the inner ring and the cage cantering surface because of the fluid dynamic pressure effect, respectively; M_{cx}' is the frictional moment generated on the cage surface by the distributed pressure of the lubricant fluid dynamic pressure film; M_{CDO} and M_{CDS} are the resistances of the outer surface and end face of the cage caused by the shear of the surrounding air-oil mist mixture; their expressions for the forces are given in the literature [26]. The nonlinear dynamic differential equations of the cage are

$$\begin{cases} m_c \ddot{y}_c = \sum_j^{RN} \left(N_{rj}^c \sin \varphi_j + F_{rj}^c \cos \varphi_j \right) + F_{cy}' \cos \psi_c + F_{cz}' \sin \psi_c - G^c, \\ m_c \ddot{z}_c = \sum_j^{RN} \left(N_{rj}^c \cos \varphi_j - F_{rj}^c \sin \varphi_j \right) + F_{cy}' \sin \psi_c - F_{cz}' \cos \psi_c, \\ J_{cx} \dot{\omega}_{cx} = \sum_j^{RN} \left(F_{rj}^c \frac{D_w}{2} \right) - M_{cx}' - M_{CDO} - M_{CDS}, \\ J_{cy} \dot{\omega}_{cy} = \sum_j^{RN} \left(-M_{rj}^c \cos \varphi_j \right), \\ J_{cz} \dot{\omega}_{cz} = \sum_j^{RN} \left(M_{rj}^c \sin \varphi_j \right), \end{cases} \tag{19}$$

where m_c is the mass of cage; $\ddot{y}_c$ and $\ddot{z}_c$ are the displacement accelerations of the cage's mass centre in the inertial coordinate system; J_{cx}, J_{cy}, and J_{cz} are the rotational inertias of cage in the inertial coordinate system; $\dot{\omega}_{cx}$, $\dot{\omega}_{cy}$, and $\dot{\omega}_{cz}$ are the angular accelerations of the cage in the inertial coordinate system; G^c is the gravity of cage; and RNis the number of rollers.

6. Dynamic Differential Equations of the Inner Ring

In addition to the normal force, friction force, and torque of the internal elements, the inner ring is subjected to an external radial load. The nonlinear dynamic differential equations of the inner ring are

$$\begin{cases} m_i\ddot{x}_i = \sum_j^{RN}\left(Q_{ezj}^X - F_{cwxj} + \mu_{sj}^i N_{rj}^i\right), \\ m_i\ddot{y}_i = \sum_j^{RN}\left(N_{rj}^i\cos\varphi_j + T_{rj}^i\sin\varphi_j + Q_{ezj}^Y\cos\varphi_j + Q_{e\theta j}\sin\varphi_j\right) - F_r - G^i, \\ m_i\ddot{z}_i = \sum_j^{RN}\left(-N_{rj}^i\sin\varphi_j + T_{rj}^i\cos\varphi_j - Q_{ezj}^Y\sin\varphi_j + Q_{e\theta j}\cos\varphi_j\right), \\ J_{ix}\dot{\omega}_{ix} = \sum_j^{RN}\left(T_{rj}^i\frac{D_w}{2} + M_{ezj}\right), \\ J_{iy}\dot{\omega}_{iy} = \sum_j^{RN}\left(M_{Trj}^i\sin\varphi_j - M_{erj}\cos\varphi_j - M_{eej}\sin\varphi_j + M_{e\theta j}\cos\varphi_j\right), \\ J_{iz}\dot{\omega}_{iz} = \sum_j^{RN}\left(M_{Trj}^i\cos\varphi_j + M_{erj}\sin\varphi_j - M_{eej}\cos\varphi_j - M_{e\theta j}\sin\varphi_j\right), \end{cases} \tag{20}$$

where m_i is the mass of the inner ring; $\ddot{y}_i$ and $\ddot{z}_i$ are the displacement accelerations of the inner ring mass centre in the inertial coordinate system; J_{ix},J_{iy}, and J_{iz} are the rotational inertias of the inner ring in the inertial coordinate system; $\dot{\omega}_{ix}$, $\dot{\omega}_{iy}$, and $\dot{\omega}_{iz}$ are the angular accelerations of the inner ring in the inertial coordinate system; F_r is the radial load; and G^i is the gravity of inner ring.

7. Calculation of the *PV* Value and Slip Speed of the Roller

7.1. Calculation of the PV Value of the Roller End Face. If the roller does not exhibit the dynamic unbalance mass, its skew angle in the operation process is very small, and the friction between roller end face and inner ring rib is not considered to occur. However, when the roller exhibits a certain amount of dynamic unbalance mass, its oscillation in the raceway causes a significant contact between the roller end face and inner ring rib. According to the Archard wear model [28], the wear rate of the material is proportional to the contact pressure p and sliding velocity V. Therefore, the PV value between the roller end face and inner ring rib is used to evaluate the wear degree of roller end face. According to the contact geometry and relative motion relationship between roller end face and inner ring rib, the PV value of the jth roller end face can be obtained as follows:

$$PV_{erj} = P_{rj}V'_{erj}, \tag{21}$$

where P_{rj} is the contact stress for the jth roller end face and inner ring rib, and it can be determined using the following equation:

$$P_{rj} = \frac{3Q_{ez}}{(2\pi ab)}, \tag{22}$$

where a and b are the long semiaxis and the short semiaxis of contact ellipse, respectively:

$$\begin{cases} a = \left[\frac{6k^2\Gamma R_{eff}Q_{ez}}{(\pi E')}\right]^{1/3}, \\ b = \left[\frac{6\Gamma R_{eff}Q_{ez}}{(\pi kE')}\right]^{1/3}. \end{cases} \tag{23}$$

V'_{erj} is the relative speed of contact point between the jth roller end face and inner ring rib:

$$V'_{rj} = \left|v_{\mathrm{i}} - v_{\mathrm{r}}\right|. \tag{24}$$

7.2. Calculation of Slip Speed of the Roller Working Surface. When the roller has a dynamic unbalance mass, the roller oscillates significantly, resulting in a large relative sliding between its working surface and the raceway, intensifying the frictional wear of the roller. However, the additional contact stress between the roller and raceway is relatively small due to the roller's dynamic unbalance mass; therefore, the slip speed is used to evaluate the wear degree of roller's working surface, and it can be expressed as

$$V_{rj} = abs\left[\left(\omega_{ix}\times\frac{d_i}{2} - \omega_{rxj}\right)\times\left(R_{ro} - \omega_{rsxj}\times\frac{D_w}{2}\right)\right], \tag{25}$$

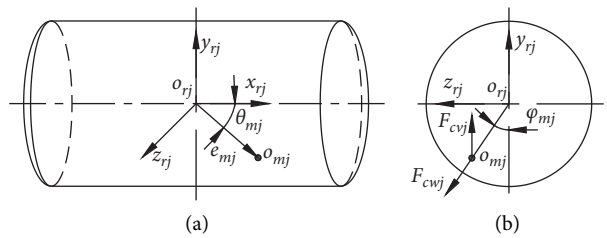

Figure 4: Schematic diagram of the jth roller's dynamic unbalance mass.

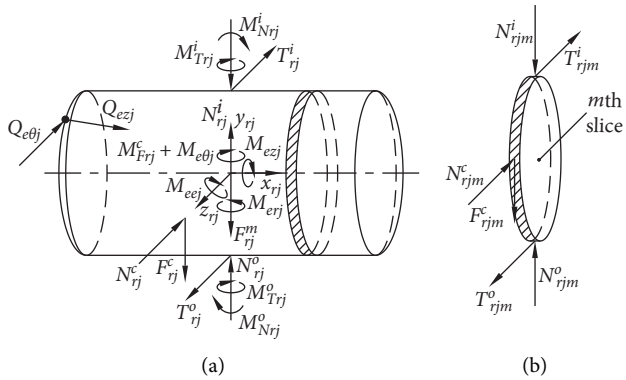

Figure 5: Schematic diagram of forces acting on the jth roller.

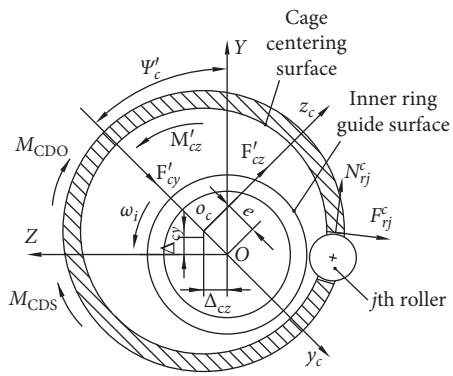

Figure 6: Schematic diagram of cage forces.

where V_{rj} is the jth roller's slip speed; ω_{ix} and ω_{rxj} are the angular velocities of the inner ring and the jth roller in the inertial coordinate system, respectively; ω_{rsxj} is the spin angular velocity of the jth roller; R_{ro} is the distance between the jth roller's centre and the inner ring's centre along the radial direction in the inertial coordinate system; and d_i is the inner ring raceway diameter.

8. Interpretation of Results

The dynamic differential equations (19)–(21) of cylindrical roller bearing are solved by GSTIFF (Gear Stiff) integer algorithm with variable step [29]. The PV value and the slip speed were obtained. The main parameters of cylindrical roller bearing are listed in Table 1.

Due to the influence of machining factors, the size of roller's chamfer is the most likely reason to cause the dynamic unbalance mass. Therefore, the dynamic unbalance mass of the roller was placed in this position of the roller's chamfer, and the dynamic unbalance mass was analysed in the range of 0.06–0.11 g. It was assumed that the dynamic unbalance mass is located at the right chamfer position of the roller.

Table 1: Main parameters of bearing.

Parameter	Parameter values
Bearing inner diameter (mm)	50
Bearing outer diameter (mm)	75
Bearing width (mm)	16
Roller diameter (mm)	6
Cage guide method	Inner ring guide

9. Effect of Bearing Condition on the PV Value and Slip Speed

Assuming that the axial clearance of bearing was 0.03 mm, the circumferential clearance of cage pocket was 0.2 mm, the angle of the inner ring rib was 0.3°, and the crowned radius of roller end face was 300 mm. The following bearing operating parameters were varied in order to study their effect on the PV value and its slip speed under the different dynamic unbalance mass.

9.1. Influence of Radial Load on the PV Value and Slip Speed. The effect of radial load on the PV value and slip speed was analysed. For the inner ring speed of 30000 r/min, the PV value and its slip speed varying with the radial load are shown in

Figure 7, where L and R represent the PV values of the left end face and the right end face of the roller, respectively.

Figure 7 indicates that the PV value and slip speed increase with the increase in roller's dynamic unbalance mass, and the PV value of the right end face is larger. This is because of the increase in centrifugal force, the increase in roller skew angle, the increase in roller swing speed, and aggravation of roller slip. In addition, the increase in the skew angle of the roller increases the force between roller end face and the inner ring's rib increase. This caused the PV value to increase with an increase in the roller's dynamic unbalance mass. Because the roller is subjected to the unilateral centrifugal force caused by the dynamic unbalanced mass, the PV value of the roller end face where the dynamic unbalanced mass is located is larger.

When the dynamic unbalance mass of the roller is eliminated, the PV value of the roller end face does not change noticeably with the increase in radial load, and the slip speed of the roller decreases with the increase in radial load and tends to be moderate when the load exceeds 5000 N. This is because the bearing with a pure radial load has both a bearing area and a nonbearing area during operation. In the nonbearing zone, the correlation between the running state of the roller itself and the radial load is small, and the limit of the roller swing is weak; that is, the change in the PV value is not clear. In the bearing area, the larger the radial load is, the greater the force the ring is subjected to and the stronger the drag force of the inner ring on the roller is. This leads to a higher cage speed, that is, a higher roller rotation speed and a relative decrease in the roller's slip speed. After the radial load exceeded 5000 N, the actual speed of the roller was close to the theoretical value, and the roller's slip speed tended to be stable.

9.2. Effect of the Inner Ring Speed on Roller End PV and Slip Speed. For the radial load of 3000 N, the PV value and its slip speed varying with the bearing speed are shown in Figure 8.

From Figure 8, when the roller's dynamic unbalance mass is certain, the PV value and the slip speed increase with a rise in the inner ring speed. With an increase in the inner ring speed, the rotational speed of roller increases, the centrifugal force produced by the dynamic unbalance mass rises, the degree of roller skew increases, the force between the roller end face and the inner ring rib will increase, and the roller slip speed will be faster. Therefore, the PV value increases with the inner ring speed and the dynamic unbalance mass, and the impact is more significant. In contrast, with an increase in the inner ring speed and centrifugal force, the drag ability of the inner ring to the roller is weakened, the roller swing ability is enhanced, the contact force and friction force between the roller end face and inner ring rib increases, and the slip speed of the roller increases.

10. Effect of Bearing Structure Parameters on the PV Value and Slip Speed

When the inner ring speed was 30000 r/min, the radial load was 3000 N, and the influence of the bearing structure parameters on the PV value and slip speed under the different roller's dynamic unbalance mass was analysed.

10.1. Effect of Axial Clearance of Bearing on the PV Value and Slip Speed. For the cage pocket circumferential clearance of 0.2 mm, the angle of inner ring rib of 0.3°, and the crowned radius of roller end face of 300 mm, the PV value and its slip speed changing with bearing axial clearance are shown in Figure 9.

Figure 9 shows that when the roller's dynamic unbalance mass is certain, the PV value increases with the increase of the axial clearance, and the roller's slip speed decreases with the increase of the axial clearance, both of which tend to flatten after the axial clearance exceeds 0.05 mm. This was because when the axial clearance is small, the roller contact with the inner ring rib greatly inhibits the skew of the roller and reduces the speed of the roller swing. As a result, the PV value was reduced, but this inhibition will weaken the roller's normal rolling ability and increase the roller's slip speed. When the clearance exceeds 0.05 mm, the inhibition of the roller skew by the inner ring rib is weakened, and the inhibition ability of the cage to the roller skew was relatively improved; that is, the force between the roller and the cage was increased (which may cause the violent friction between the cage and the roller) [22]. The roller swing will not continue to enhance the PV value and slip speed to maintain a steady change. Considering the dynamic unbalance mass of roller, there was a reasonable axial clearance range of bearing (0.03–0.05 mm) which makes the roller slip speed smaller when the PV value is not too large.

10.2. Effect of Circumferential Clearance of Cage Pocket on the PV Value and Slip Speed. For the bearing axial clearance of 0.03 mm, the angle of inner ring rib of 0.3°, and the crowned radius of roller end face of 300 mm, the PV value and its slip speed with the cage pocket circumferential clearance change as shown in Figure 10.

Figure 10 shows that when the roller's dynamic unbalance mass was certain, the PV value and the slip speed increased with the circumferential clearance of cage pocket and tended to flatten out after the circumferential clearance exceeded approximately 0.35 mm. When the circumferential clearance was small, the swing of the roller in the pocket was limited by the front and rear beam of the cage, its inhibition on the swing ability of the roller was greater, and the contact deformation between the roller and the inner ring rib was smaller. At this stage, with the increase of circumferential clearance, the ability of the roller swing was significantly enhanced, and the force between roller end face and inner ring rib increased gradually, making the PV value and its slip speed increase significantly. When the circumferential clearance of the pocket exceeded 0.35 mm, the swing of the roller was limited by the unilateral beam, the inhibition effect of the cage on the skew of the roller was weakened, and the swing ability of the roller was restored. The change of the PV value and slip speed tended to stabilize. Therefore, considering the roller's dynamic unbalance mass, to ensure that the roller and the cage beam collision force would not be too large, smaller cage pocket circumferential clearance should be chosen.

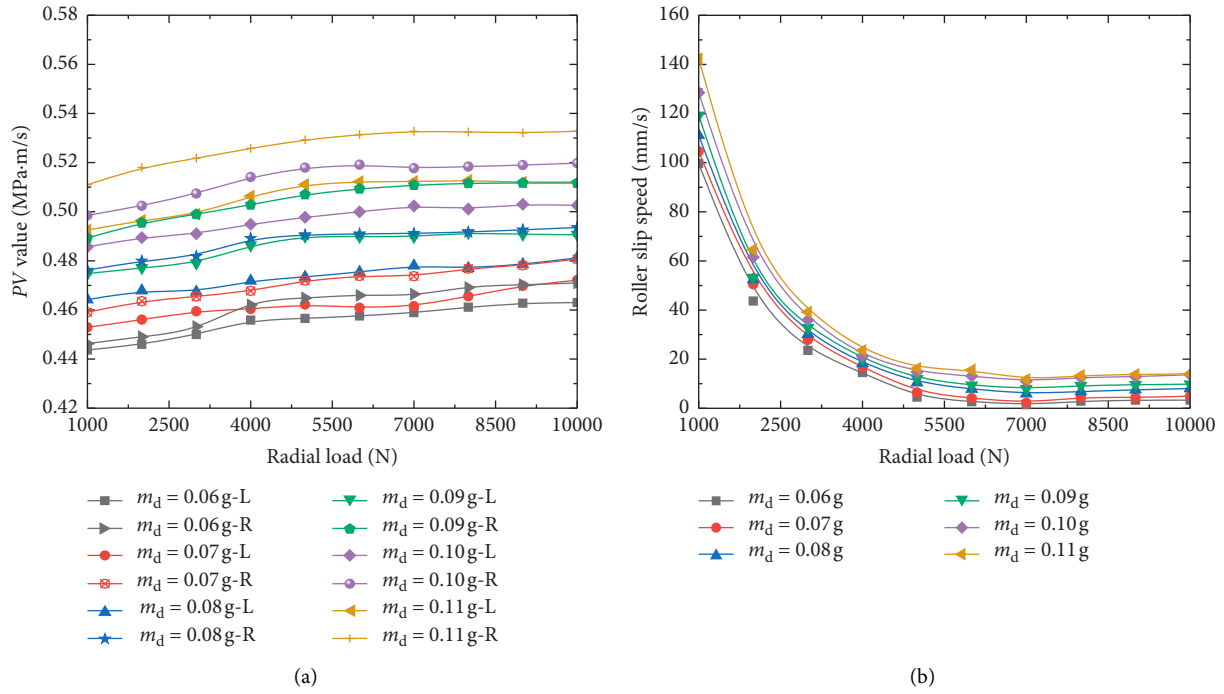

FIGURE 7: Variation of *PV* values and its slip speed with the radial load. (a) Change of *PV* value. (b) Change of roller slip speed.

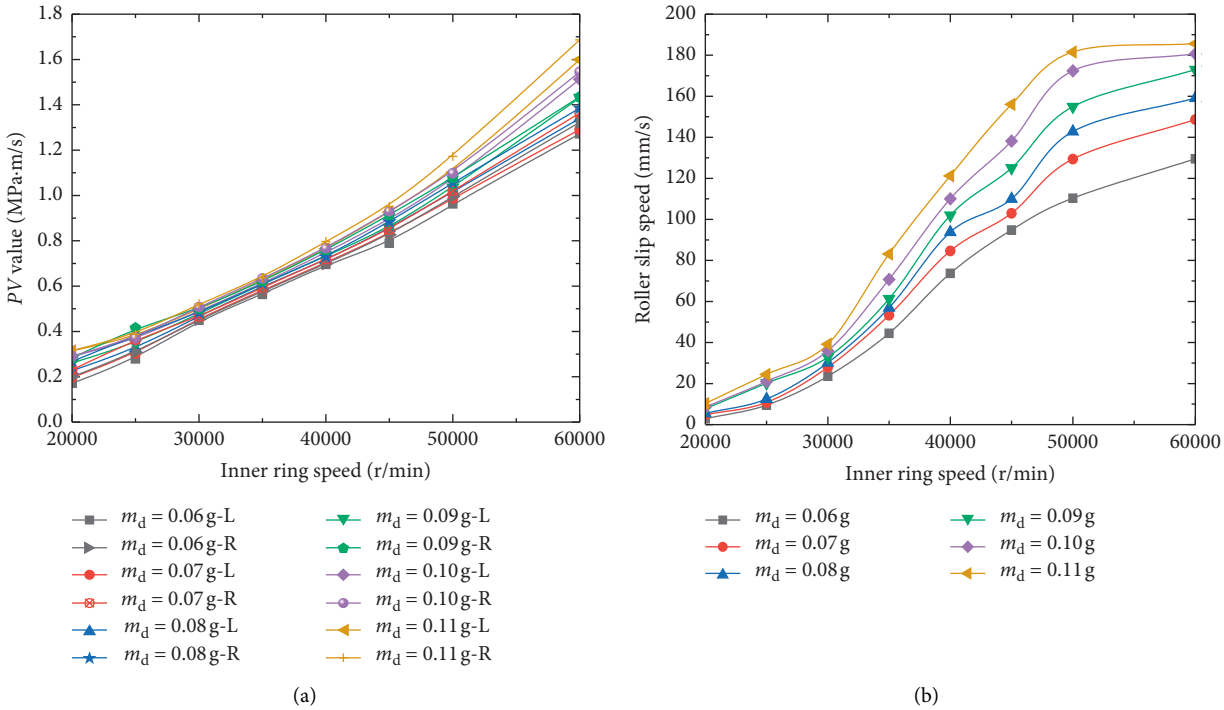

FIGURE 8: Variation of *PV* value and its slip speed with the inner ring speed. (a) Change of the *PV* value. (b) Change of the roller's slip speed.

10.3. Effect of Angle of Inner Ring Rib on the PV Value and Slip Speed. For the bearing axial clearance of 0.03 mm, the frame pocket hole circumferential clearance of 0.2 mm, and the crowned radius of roller end face of 300 mm, the *PV* value and its slip speed with the angle of inner ring rib are shown in Figure 11.

Figure 11 shows that when the roller's dynamic unbalance mass is certain, the *PV* value decreases first and then increases with the increase of the angle of inner ring rib, and the minimum value appears when the angle is 0.55°. The slip speed of the roller increases when the angle of inner ring rib increases, and the slip speed increases sharply when the

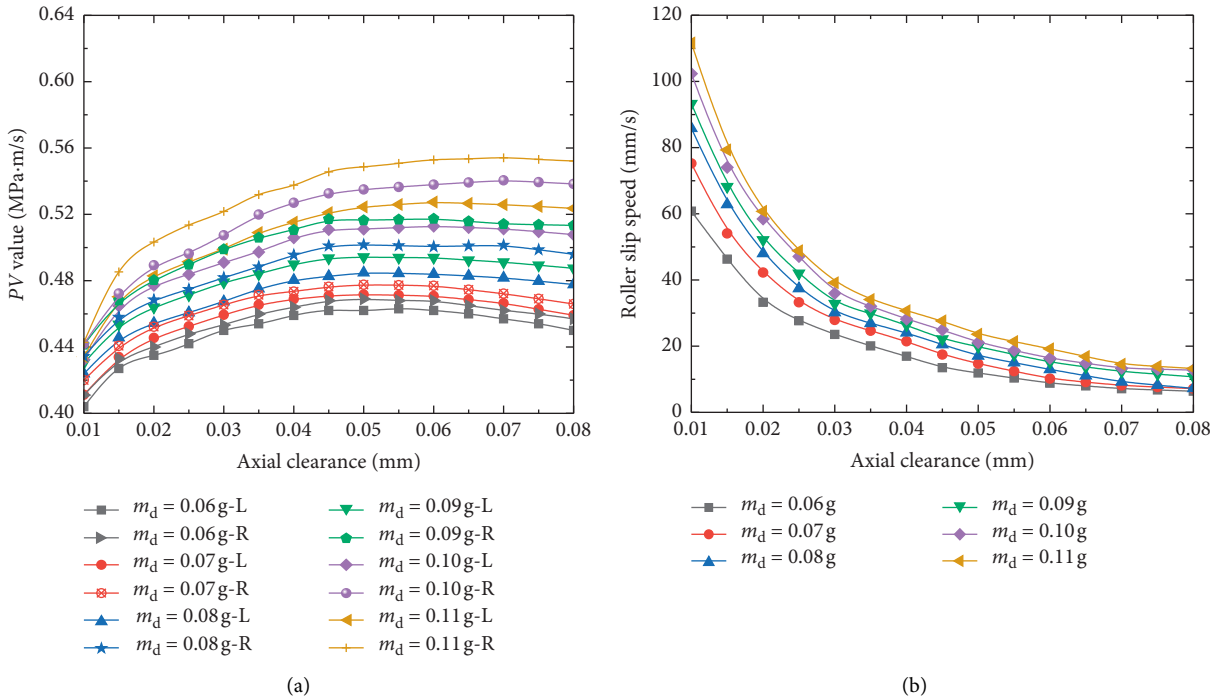

FIGURE 9: Variation of *PV* value and its slip speed with the axial clearance. (a) Change of the *PV* value. (b) Change of the roller slip speed.

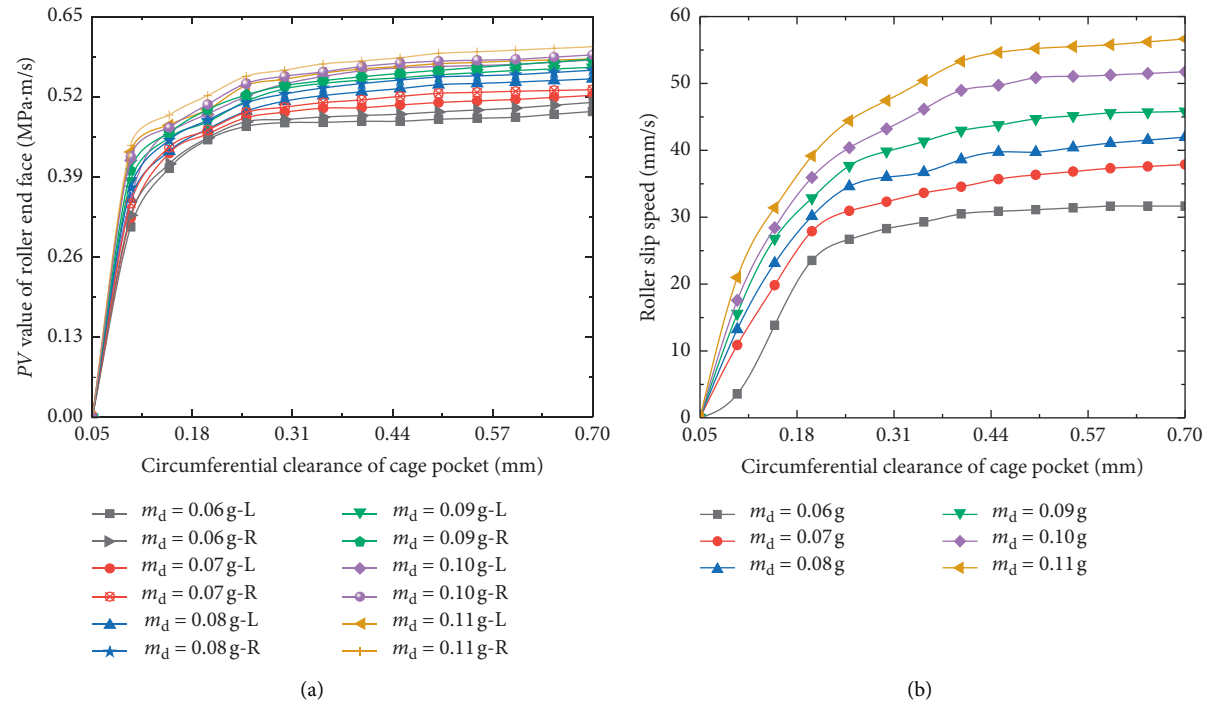

FIGURE 10: Variation of *PV* value and its slip speed with the cage pocket circumferential clearance. (a) Change of the *PV* value of the roller end face. (b) Change of the roller slip speed.

angle is 0.4°–0.7°. This was because when the angle of the inner ring rib is small, the more the angle increases, the farther the contact point between the roller end face and the rib is from the roller axis; that is, the smaller the distance between the contact point and the crowned centre of the roller end face in the direction of the roller axis, the larger the skewing angle of the roller; at this time, the axial clearance and the circumferential clearance of the cage pocket are unchanged. Under the limitation of the cage beam, the contact force between the roller end face and the inner ring

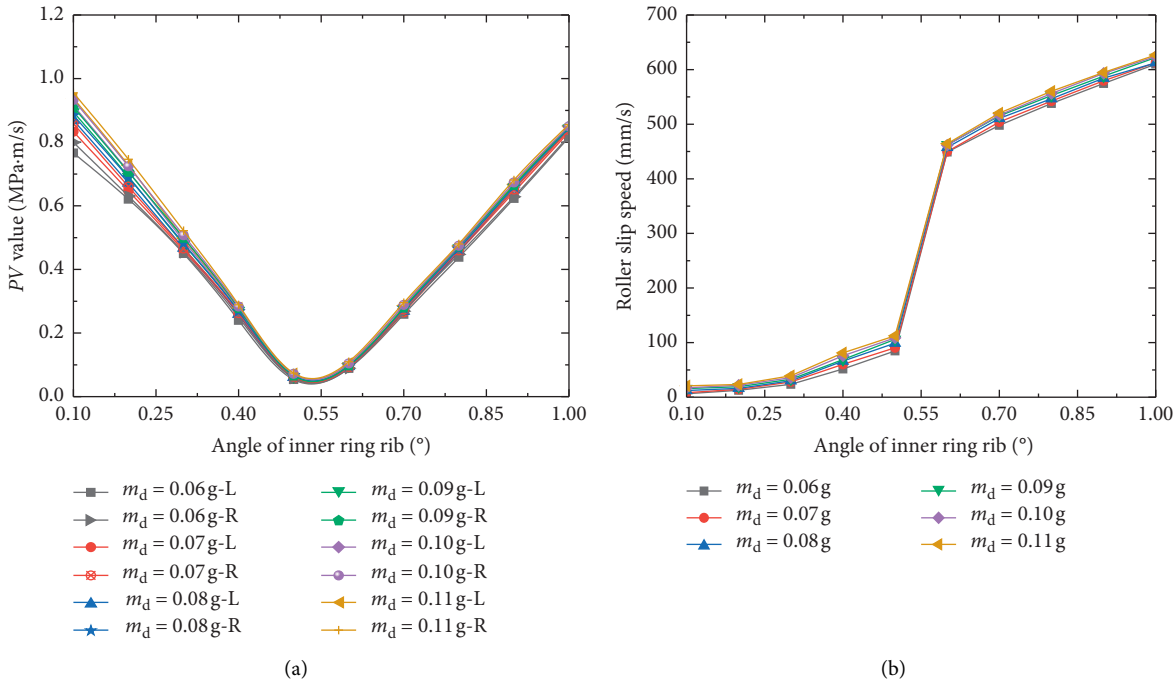

Figure 11: Variation of the *PV* value and its slip speed with the angle of inner ring rib. (a) Change of the *PV* value. (b) Change of the roller slip speed.

rib decreases, and the *PV* value also decreases. When the angle of inner ring rib was more than 0.55°, the force acted on the roller end face was weaker, the roller swing speed increases, and the *PV* value is not only affected by the contact stress but also related to the relative velocity of the contact point. The *PV* value also begins to increase. In contrast, in the process of increasing the angle, the roller's slip speed increased continuously because the roller swing ability was always improving. When the angle was in the range of 0.4°–0.7°, the force of the inner ring acting on the end face of the roller was weak, the limitation ability of the cage beam to the skew of the roller was moderate, and the slip speed of the roller increased sharply. When the angle was large, the limitation ability of cage beam to roller's skew was stronger, and the increase of roller's slip speed was slowed down. Therefore, considering the dynamic unbalance mass of roller, when the height of the inner ring rib was certain, there was a reasonable angle of the inner ring rib. The bearing studied in this paper is 0.4°–0.45°, which makes the *PV* value and the slip speed smaller.

10.4. Effect of the Crowned Radius of Roller End Face on the PV Value and Slip Speed. For the axial clearance of the bearing of 0.03 mm, the circumferential clearance of the cage pocket was 0.2 mm and the angle of inner ring rib was 0.3°. The *PV* value and its slip speed varying with the crowned radius of roller end face are shown in Figure 12.

Figure 12 shows that when the dynamic unbalance mass of roller was fixed, the *PV* value decreased first and then increased with the increase of the crowned radius of roller end face, and the minimum value appeared when the crowned radius was 550 mm. The roller's slip speed increases with the increase of the crowned radius, and the roller's slip speed increases sharply when the crowned radius is 500–600 mm. As the crowned radius increases, the greater the distance between the contact point and the crowned centre of the roller in the direction of the roller axis, the smaller the theoretical skewing angle of the roller, and the increase of the contact load between the roller end face and the inner ring rib will decrease the contact stress, so the *PV* value will decrease with the increase of the crowned radius. In contrast, the effect of inner ring rib on roller's skew was increased with the increase of crowned radius, and the drag force of inner ring rib on roller end face will inhibit roller rotation. Therefore, the roller slip speed always increases in the process of increasing the crowned radius. When the crowned radius was in the range of 500–600 mm, the limiting ability of the cage beam to the roller skew was moderate, and the slip speed of the roller increased sharply. When the crowned radius was large, the contact load between roller end face and inner ring rib was larger. Due to the contact angle being small, the collision between the cage beam and the roller will play the role of correcting roller attitude. The increase of roller slip speed is slowed down. Therefore, considering the dynamic unbalance mass of the roller, synthesising the geometric relationship between the angle of inner ring rib and the crowned radius, the crowned radius of roller end face in the range of 450–500 mm is selected.

11. Test Verification

Based on the aforedescribed theoretical analysis, it can be concluded that the roller dynamic unbalance mass caused by the inconsistent chamfering size at both ends of the roller

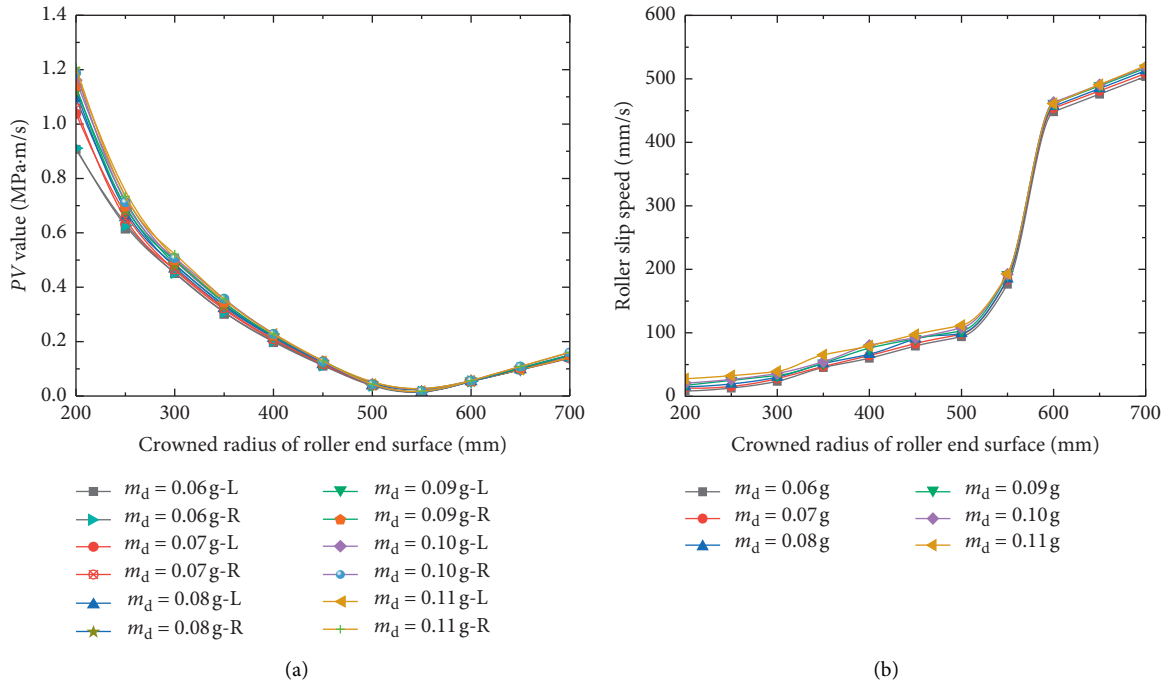

Figure 12: Variation of *PV* value and its slip speed with the crowned radius of the roller end face. (a) Change of the *PV* value. (b) Change of the roller slip speed.

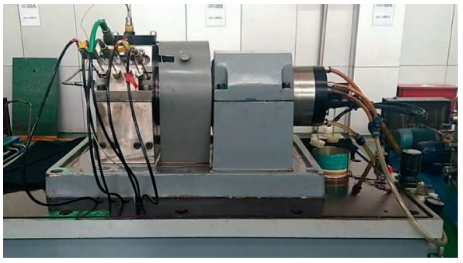

Figure 13: ZYS-103 high-speed and high-temperature bearing performance testing machine.

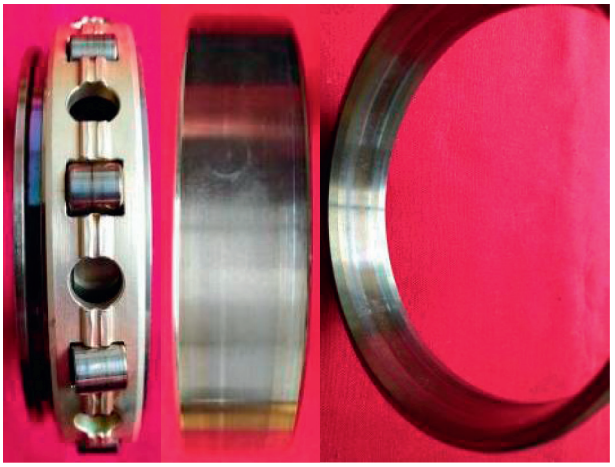

Figure 14: Appearance of the tested bearing.

Table 2: Accuracy item of the tested bearing.

Serial number	Radial clearance (μm)	Axial clearance (μm)	Outer raceway (μm)		Roller (μm)		
			Roundness	Roughness	Roundness	Roughness	Diameter deviation
Standard value	60–80	30–50	≤2	0.063	0.4	0.125	−10–+5
1	63	40–50	0.7	0.04	0.06	0.074	−1-−2
2	64	40–50	0.65	0.061	0.08	0.058	−1-−−2
3	62	40–50	0.45	0.045	0.12	0.053	−2-−3
4	63	40–50	0.61	0.053	0.20	0.046	−2-−3

and the excessive axial clearance of the bearing and are the main causes of abnormal wear on the working surface and end face of the roller; therefore, the axial clearance of the bearing is controlled within 0.03–0.05 mm, the angle of the inner ring rib is controlled within 0.4°–0.45°, the chamfering size of the roller is controlled at 0.5 ± 0.05 (0.5 ± 0.1 mm is the origin value), and the roller end face is still flat.

Performance test of four sets of improved bearings using a ZYS-103 high-speed and high-temperature bearing performance testing machine is in Figure 13. The test load, velocity, and time of bearing are 3000 N, 30000 r/min, and 500 hours, respectively. The appearance of the improved bearing after the test is shown in Figure 14 and it can be compared with that of the unimproved bearing shown in Figure 1. Some accuracy indices are listed in Table 2, it can be seen from Table 2 that the main precision index of the bearing after the test is still within the range of the design standard value, and some indexes are slightly improved. The improved bearing passed the performance test.

12. Conclusion

(1) The large amount of roller's dynamic unbalance mass and the deviation of the bearing axial clearance are the main causes of abnormal wear on the roller working surface and end faces of cylindrical roller bearing. The larger roller's dynamic unbalance mass leads to the larger *PV* value and slip speed; therefore the roller's dynamic unbalance mass must be confined in a low level.

(2) The *PV* value and its slip speed increased with the increase in roller dynamic unbalance mass, and the *PV* value of the roller end face where the dynamic unbalance mass is located in was larger. With an increase in the radial load, the *PV* value did not change significantly, the slip speed of roller decreased, and it tended to be gentle after the load exceeded 5000 N. With an increase in the inner ring speed, the *PV* value and its slip speed increased.

(3) A smaller axial clearance was found to effectively suppress the *PV* value, but it did cause an increase in the roller slip speed. A reasonable axial clearance range was found to exist. The axial clearance of bearing studied in this paper is 0.03–0.05 mm, which makes the roller slip speed smaller when the *PV* value is not too large.

(4) Both the *PV* value and the roller slip speed increased with the increase of the circumferential clearance of the cage pocket. When the circumferential clearance of the pocket exceeds 0.35 mm, the *PV* value and slip speed change more smoothly with the clearance. Considering the roller dynamic unbalance mass, a smaller circumferential clearance of cage pocket should be chosen.

(5) The *PV* value decreased and then increased with an increase in the angle of the inner ring rib and the crowned radius of the roller end face, reaching a minimum at 0.55° and 550 mm, respectively. The roller slip speed increased with the increase in the angle of the inner ring rib and the crowned radius of the roller end face, increasing sharply at 0.4°–0.7° and 500–600 mm, respectively. A reasonable range of the angle of the inner ring rib and the crowned radius of the roller end face was found to exist. The bearings studied in this paper were 0.4°–0.45° and 450–500 mm, respectively, which reduced the *PV* value and the roller slip speed.

Data Availability

The data used to support the findings of this study are available from the corresponding author upon request.

Conflicts of Interest

The authors declare that they have no conflicts of interest.

Acknowledgments

This research was financially supported by Youth Program of the National Natural Science Foundation of China (51905152) and China Postdoctoral Science Foundation (2020M671276).

References

[1] L. Jing, "A dynamic modelling method of a rotor-roller bearing-housing system with a localized fault including the additional excitation zone," *Journal of Sound and Vibration*, vol. 469, Article ID 115144.

[2] J. Liu, Y. Xu, and G. Pan, "A combined acoustic and dynamic model of a defective ball bearing," *Journal of Sound and Vibration*, vol. 501, no. 1, Article ID 116029, 2021.

[3] Z. Yang, S. Yu, and X. Chen, "Analysis of roller end wear question for high speed short cylindrical roller bearing," *Journal of Harbin Bearing*, vol. 30, no. 2, pp. 44–45, in Chinese, 2009.

[4] Y. Shi and B. Li, "Numerical simulation of wearing for cylindrical roller bearing," *Lubrication Engineering*, vol. 34, no. 11, pp. 23–26, 2009, in Chinese.

[5] Y. Shi, Q. Jiang, and B. Li, "Numerical simulation of wear process and reliability life for cylindrical roller bearing," *Lubrication Engineering*, vol. 35, no. 2, pp. 30–34, 2011, in Chinese.

[6] J. Yao, J. Tan, and B. Yang, "Kinetic simulation on ADAMS and experimental study of wear failure of cylindrical roller bearings," *China Mechanical Engineering*, vol. 25, no. 17, pp. 2327–2330, 2014, in Chinese.

[7] Q. Yu, G. Yan, J. Zhang, and P. Gong, "Analysis on wear mechanism for roller end face and inner ring rib of cylindrical roller bearings," *Bearing*, no. 3, pp. 7–9, 2019, in Chinese.

[8] L. Wen, *Analysis on Roller End Face Wear-Out Failure in Aero-Engine Intershaft Bearings and Improvement Design of Bearing*, Harbin Institute of Technology, Harbin, China, 2019, in Chinese.

[9] S. Aditya, M. Amarnath, and P. K. Kankar, "Failure analysis of a grease-lubricated cylindrical roller bearing," *Procedia Technology*, vol. 14, no. 14, pp. 59–66, 2014.

[10] Q. Han, X. Li, and F. Chu, "Skidding behavior of cylindrical roller bearings under time-variable load conditions," *International Journal of Mechanical Sciences*, vol. 135, pp. 203–214, 2018.

[11] Q. Zhang, J. Luo, X.-y. Xie, J. Xu, and Z.-h. Ye, "Experimental study on the skidding damage of a cylindrical roller bearing," *Materials*, vol. 13, no. 18, p. 4075, 2020.

[12] F. Li, W. Hu, Q. Meng, Z. Zhan, and F. Shen, "A new damage-mechanics-based model for rolling contact fatigue analysis of cylindrical roller bearing," *Tribology International*, vol. 120, pp. 105–114, 2018.

[13] W. Tu, W. Yu, Y. Shao, and Y. Yu, "A nonlinear dynamic vibration model of cylindrical roller bearing considering skidding," *Nonlinear Dynamics*, vol. 103, no. 3, pp. 2299–2313, 2021.

[14] A. Leblanc, D. Nelias, and C. Defaye, "Nonlinear dynamic analysis of cylindrical roller bearing with flexible rings," *Journal of Sound and Vibration*, vol. 325, no. 1-2, pp. 145–160, 2009.

[15] Y. S. Wang, N. N. Jin, and H. F. Zhu, "Analysis on dynamic characteristics of high speed cylindrical roller bearing," *Key Engineering Materials*, vol. 480-481, pp. 980–985, 2011.

[16] C. Yongcun, D. Sier, Z. Wenhu, and C. Guoding, "The impact of roller dynamic unbalance of high-speed cylindrical roller bearing on the cage nonlinear dynamic characteristics," *Mechanism and Machine Theory*, vol. 118, pp. 65–83, 2017.

[17] Y. Cui, S. Deng, R. Niu, and G. Chen, "Vibration effect analysis of roller dynamic unbalance on the cage of high-speed cylindrical roller bearing," *Journal of Sound and Vibration*, vol. 434, pp. 314–335, 2018.

[18] X. Sun, S. Deng, G. Chen, and W. Zhang, "Analysis of cage's stability in a cylindrical roller bearing with elastic support," *Journal of Aerospace Power*, vol. 33, no. 2, pp. 487–496, 2018, in Chinese.

[19] X. Sun, W. Zhang, and H. Tian, "Theoretical analysis of cylindrical roller bearing with flexible rings mounted in groove elastic support," *Journal of Advanced Mechanical Design, Systems, and Manufacturing*, vol. 14, no. 7, Article ID JAMDSM0102, 2020.

[20] X. Liu, X. Bai, J. Cui, and P. Yang, "Thermal elastohydrodynamic lubrication analysis for tilted and skewed rollers in cylindrical roller bearings," *Proceedings of the Institution of Mechanical Engineers - Part J: Journal of Engineering Tribology*, vol. 230, no. 4, pp. 428–441, 2015.

[21] W. Zhang, S. Deng, G. Chen, and Y. Cui, "Study on the impact of roller convexity excursion of high-speed cylindrical roller bearing on roller's dynamic characteristics," *Mechanism and Machine Theory*, vol. 103, pp. 21–39, 2016.

[22] P. Patra, V. H. Saran, and S. Harsha, "Non-linear dynamic response analysis of cylindrical roller bearings due to rotational speed," *Proceedings of the Institution of Mechanical Engineers - Part K: Journal of Multi-Body Dynamics*, vol. 233, no. 2, pp. 379–390, 2018.

[23] J. Zheng, S. Deng, W. Zhang et al., "Atypical failure mechanism of aero-engine mainshaft roller bearing," *Acta Aeronautica et Astronautica Sinica*, vol. 41, no. 5, in Chinese, Article ID 423347, 2020.

[24] Y. Zhao, M. Bi, and D. Shi, "Design of high speed cylindrical roller bearings based on control of roller skew," *Bearing*, no. 12, pp. 14–16, 2018, in Chinese.

[25] R. J. Kleckner, J. Pirvics, and V. Castelli, "High speed cylindrical rolling element bearing analysis "CYBEAN"f," *Journal of Lubrication Technology*, vol. 102, no. 3, pp. 380–388, 1980.

[26] S. Deng, Q. Jia, and J. Xue, *Design Theory of Rolling Bearings*, Standards Press of China, Beijing, China, 2014, in Chinese, 2nd edition.

[27] J. Yang, *Contact Mechanics Theory and Design Analysis of Rolling Bearings*, Huazhong University of Science and Technology Press, Wuhan, China, 2018, in Chinese.

[28] J. F. Archard, "Contact and rubbing of flat surfaces," *Journal of Applied Physics*, vol. 24, no. 8, pp. 981–988, 1953.

[29] C. Gear, "Simultaneous numerical solution of differential-algebraic equations," *IEEE Transactions on Circuit Theory*, vol. 18, no. 1, pp. 89–95, 1971.